

Marquette University
e-Publications@Marquette

Mechanical Engineering Faculty Research and
Publications

Mechanical Engineering, Department of

3-15-2008

Mesoscale Calculations of the Dynamic Behavior of a Granular Ceramic

John Borg

Marquette University, john.borg@marquette.edu

Tracy J. Vogler

Sandia National Laboratories

Accepted version. *International Journal of Solids and Structures*, Vol. 45, No. 6 (March 15, 2008):
1676-1696. [DOI](#). © 2007 Elsevier Ltd. Used with permission.

Marquette University

e-Publications@Marquette

Mechanical Engineering Faculty Research and Publications/College of Engineering

This paper is NOT THE PUBLISHED VERSION; but the author's final, peer-reviewed manuscript. The published version may be accessed by following the link in the citation below.

International Journal of Solids and Structures, Vol. 45, No. 6 (March 15, 2008): 1676-1696. [DOI](#). This article is © Elsevier and permission has been granted for this version to appear in [e-Publications@Marquette](#). Elsevier does not grant permission for this article to be further copied/distributed or hosted elsewhere without the express permission from Elsevier.

Mesoscale Calculations of The Dynamic Behavior of a Granular Ceramic

John P. Borg

Marquette University, Department of Mechanical Engineering, Milwaukee, WI

Tracy J. Vogler

Sandia National Laboratories, Albuquerque, NM

Abstract

Mesoscale calculations have been conducted in order to gain further insight into the dynamic compaction characteristics of granular ceramics. The primary goals of this work are to numerically determine the shock response of granular tungsten carbide and to assess the feasibility of using these results to construct the bulk material Hugoniot. Secondary goals include describing the averaged compaction wave behavior as well as characterizing wave front behavior such as the strain rate versus stress relationship and statistically describing the laterally induced velocity distribution. The mesoscale calculations were able to accurately reproduce the experimentally determined Hugoniot slope but under predicted the zero pressure shock speed by 12%. The averaged compaction wave demonstrated an initial transient stress followed by asymptotic behavior as a

function of grain bed distance. The wave front dynamics demonstrate non-Gaussian compaction dynamics in the lateral velocity distribution and a power-law strain rate–stress relationship.

Keywords

Shock compaction, Granular materials, Mesoscale simulations, Ceramics, Porosity

1. Introduction

The bulk response of a rapidly compacted granular material is not well understood and is a current active area of research. The compaction of granular materials is of great interest when developing an understanding of processes such as powder metallurgy, geo-physical flows, and ignition mechanisms in energetic materials. In order to better understand the bulk response, computational simulations which resolve both the bulk and grain level response have been conducted, thus the term mesoscale calculations. A variety of mesoscale studies have been performed where heterogeneous grain-on-grain interactions were resolved. These studies ranged in complexity from resolving the shock and compaction interaction of tens to hundreds of grains in a two-dimensional configuration to resolving thousands of mixed material grains in a three-dimensional configuration. These studies have utilized various computational techniques such as Eulerian hydrocodes, the finite element method, or discrete elements, to resolve the dynamics of a variety of heterogeneous or granular materials, including Ti–SiC ([Benson et al., 1995b](#)), aluminum ([Nieh et al., 1996](#)), copper ([Benson, 1995a](#)), alumina ([Bourne, 2005](#)), polycrystalline copper ([Case and Horie, 2005](#)), polycrystalline iron ([Horie and Yano, 2001](#)), plastic-bonded explosives ([Milne et al., 2005](#)), steel ([Williamson, 1990](#)), Nn–Si ([Do and Benson, 2001](#)), HMX ([Benson and Conley, 1999](#), [Menikoff, 2001](#), [Lowe and Greenaway, 2005](#)), and sugar ([Baer and Trott, 2002](#)).

Small scale two-dimensional hydrocode studies involving tens of grains are typically performed to gain understanding of localized phenomena such as shock induced heating, viscous flow or dissipation as related to hot-spot formation ([Williamson, 1990](#), [Nieh et al., 1996](#), [Do and Benson, 2001](#), [Tang and Wang, 2001](#)). Larger scale studies, involving hundreds of grains, are done to resolve not only the grain dynamics, but also the bulk material response. These two-dimensional simulations have been used to successfully estimate bulk material properties of porous granular systems such as compaction density, energy deposition, zero pressure shock speed, and Hugoniot slope ([Benson, 1994](#), [Benson, 1995a](#), [Benson et al., 1995b](#); [Benson et al., 2001](#), [Crawford, 2005](#), [Hae-Jin et al., 2005](#)). These studies, specifically [Benson et al., 1995b](#), [Tong et al., 1995](#), demonstrated that the shock consolidation of granular powder mixtures was dominated by both inertia and viscoplastic properties of the matrix materials, thus corroborating predictions from various analytic porous collapse models and experimental observations ([Carroll and Holt, 1972](#), [Carroll et al., 1986](#), [Meyers et al., 1999](#)). A comprehensive numerical study of the shock compaction dynamics of granular systems, in which a parametric study of system variables such as grain material, particle geometry, porosity and stress levels, demonstrated that spatially averaged computational results are in close agreement with experimental flyer plate results ([Benson et al., 1997](#), [Nesterenko, 2001](#)). These numeric studies also included detailed descriptions of the energy deposition as a function of material properties.

During the shock consolidation process, the material response and energy coupling can be classified into either quasistatic or dynamic regimes ([Nesterenko, 2001](#)). Quasistatic compaction results in plastic deformation of the particles, void collapse and straight line particle interfaces, as would be observed in granular materials compacted in a static press. Dynamic compaction, however, results in the formation of flow structures such as jets and vortices during the plastic deformation and void collapse process. Dynamic compaction is characterized by the cascade of energy, in excess of the energy required to close the voids, down to the sub-grain level where it manifests itself in large scale deformations of the grain interfaces, inter-granular heating, thermal softening and the formation of melt layers, all of which couples in the formation of hot-spots ([Nesterenko, 2001](#)). [Benson](#)

[et al. \(1997\)](#) demonstrated that microkinetic energy, which is a measure of the energy in excess of the energy dissipated by the void collapse process, can be used as an effective metric by which the quasistatic and dynamic responses of the powder can be distinguished. In that study, the transition from quasistatic to dynamic compaction was investigated as a function of shock stress, particle size, initial porosity, material density, material strength and viscous dissipation.

With the development of massively parallel computational systems, large scale three-dimensional simulations, which include thousands of grains, have become possible ([Baer and Trott, 2002](#), [Baer, 2002](#)). These studies have focused on understanding initiation mechanisms of granular reactive materials, namely the formation of hot-spots as a result of microkinetic energy coupling. The computational requirements for such calculations have been the limiting factor with respect to performing parametric studies to investigate shock induced phenomenology over a wide range of shock loading conditions and material configurations.

The work presented here varies significantly in two ways from previous two-dimensional computational parametric studies. First, in order to better understand the compaction dynamics of granular tungsten carbide (WC) thousands of particles are resolved in two-dimensions; thus there are hundreds of particles in the shock direction. Although the computational studies mentioned above might have utilized hundreds of particles, in a two-dimensional configuration this translates to tens of particles in the shock direction. This increased spatial domain allows the compaction wave a greater distance over which to evolve compared to previous studies. This is done in order to establish a better understanding not only of the grain level interactions but also of the bulk mechanical deformation, including the initial transience within the compaction wave structure, wave quasi-steadiness, and the mechanically induced stress within both the granular and bulk material. Within the context of this enlarged computational domain, other characteristics of the compaction process such as transverse motion, shock front width, and lateral stresses are examined. Second, this study investigates a material system and loading regime where the strength of the bulk material, tungsten carbide, is comparable to the induced shock stress.

The goals of this work are to investigate grain level compaction phenomenology which should lead to a better understanding of bulk material response, i.e., resolving the bulk Hugoniot. This work seeks to investigate phenomenological behavior occurring on the order of the grain such as stress bridging, contact surface interaction, transmitted and reflected shock waves, and elastic-plastic deformation, all of which contribute to the overall bulk behavior of the material. An additional goal is to understand the dynamics which occur within the compaction wave where the material experiences high stress gradients, large deformation and particle rearrangement. In this paper, the term compaction wave will be used interchangeably with shock wave for waves traveling through the granular material. When a wave is traveling through other materials in the simulation, it will be referred to as a shock wave exclusively.

The dynamic compaction characteristics of granular tungsten carbide powder have recently been experimentally investigated using one-dimensional flyer plate experiments ([Vogler et al., 2007](#)). In these experiments the shock response was measured for WC powder with an initial volume fraction of approximately 55%. The tungsten carbide tested was manufactured by Kennametal and consisted of single crystalline grains with a characteristic length of 32 μm . [Fig. 1](#) presents a schematic of the portion of the experimental test fixture modeled in the simulations presented here, including the rigid driver plate, granular WC, buffer plate, and VISAR window.

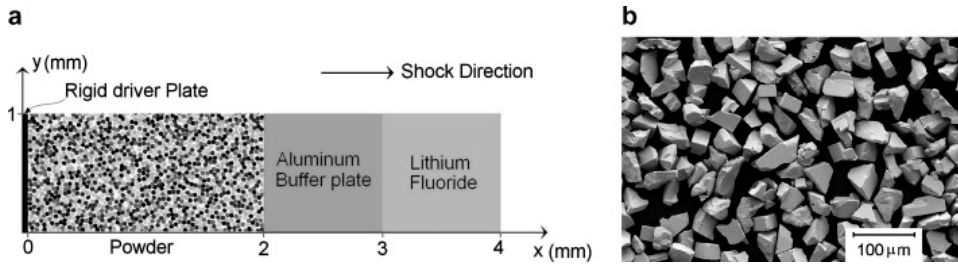


Fig. 1. (a) Two-dimensional computational geometry showing the computational domain utilized in this work and (b) SEM image of tungsten carbide particles used in the experimental study.

2. Model setup

In order to construct a material distribution which is representative of the actual random granular distribution, a numeric procedure for filling the test cell which simulates particle flow during pouring was implemented. For the numeric filling process, the granular particles are modeled as elastic circles. Circles are not representative of the WC grains shown in [Fig. 1b](#), but they do permit microstructures to be made easily and will serve as a baseline for future studies of more realistic grain shapes. During the fill process, particles are sequentially dropped into a rectangular container and, under the influence of gravity, are allowed to bounce until coming to rest. Particle interactions are modeled as elastic, frictionless collisions with damping. Once a particle comes to rest its position is fixed before the next particle is dropped. Thus, subsequent particles interact with the rigid bed of previously dropped particles. The diameter of each particle to be dropped can be selected from a statistical distribution, but the current results are for configurations with a single particle diameter. During a particle's trajectory, it may pass through the side walls of the container and appear on the other side, or it may come to rest straddling the interface. In so doing, periodic boundary conditions and periodic geometries can be generated during the fill process. The process is continued until the particles fill the domain of interest. This process creates material distributions as illustrated in [Fig. 2a](#), which is a small section of a larger domain. Notice all the particles are initially in contact with their neighboring particles and, due to the natural inclination of particles to seek the lowest potential energy under the influence of gravity, a two-dimensional body centered cubic order is established. The volume (area) fraction of the material distribution presented in [Fig. 2a](#) is on the order of 80%. In order to achieve the 55% volume fractions of the experiments, the particle diameters in [Fig. 2a](#) are reduced while holding the center coordinates of the particles fixed as suggested by [Benson \(1994\)](#). This procedure produces the material distribution presented in [Fig. 2b](#). After reducing the diameter, no particles are in contact and the arrangement remains highly ordered, especially when only a single particle diameter is present. Thus, in order to disrupt the structured particle distribution and create a more random distribution in which grains can be touching, each particle is perturbed by assigning it a small velocity in a random direction. The particles are then allowed time to move in a Brownian-like manner, bouncing off of each other for a time period equivalent to that needed to two mean free paths. After this perturbation, the material distribution presented in [Fig. 2c](#) is realized. These material realizations result in a randomized distribution of particles which may or may not be touching their nearest neighbors. This third step, i.e., randomizing the grain distribution, results in distributions which are qualitatively different than previous two-dimensional mesoscale simulations ([Benson, 1995a](#), [Benson et al., 1995b](#); [Menikoff, 2001](#)). The grains in this simulation are not distributed in a crystalline body centered like configuration, as shown in [Fig. 2b](#), nor are all the grains initially in contact. The configurations utilized in this work are between these two extremes. In addition, the grains are not bound by a matrix material, as is common with many reactive material mesoscale investigations but are instead separated by void.

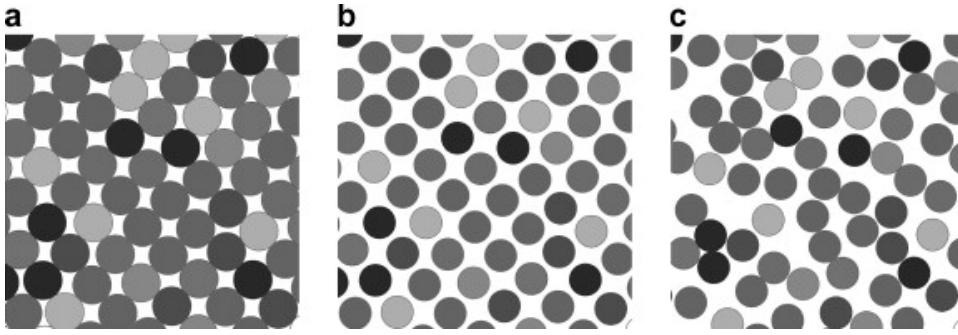


Fig. 2. Distribution of circular particles during the filling process (a) after initial dropping, (b) after shrinking particles to obtain desired volume fraction, and (c) after perturbation. Variations in particles shading is for visualization of the particles only.

Once the granular material distributions of [Fig. 2c](#) are generated, they are utilized as initial conditions in mesoscale compaction simulations using CTH ([McGlaum et al., 1990](#)), a finite volume shock physics code. CTH uses explicit time stepping to solve the equations for conservation of mass, momentum, and energy and closes the equation set with user-selected equations of state and constitutive relations for the materials in the simulation. CTH solves the governing equations in two steps: a Lagrangian step and a remap step. In the Lagrangian step, the Lagrangian forms of the governing equations are integrated across the time step. The mesh distorts to follow the material motion with no mass flux across the cell boundaries. At the end of the Lagrangian step, the remap step is performed. In this step, the distorted cells are remapped back to the Eulerian mesh and advected mass is distributed within the Eulerian mesh. As a result of the advection process, multiple materials can exist within a single computational cell; several models to accommodate cells with mixed materials have been incorporated within CTH. Because material interfaces are not resolved, CTH is not completely ideal for this application since it lacks realistic fracture, grain on grain contact dynamics, material interface tracking, etc. This inability to model grain fracture might represent a significant deficiency since fracture may play an important role in the evolution process of shocked ceramics ([Meyers et al., 1999](#)). However, simulations with Eulerian codes which resolve grain level shock interaction have been successfully used to model a variety of material behaviors ([Bourne, 2005](#), [Baer and Trott, 2002](#)). [Conley and Benson \(1999\)](#) argued that the shock dissipation associated with inter-granular friction is secondary to the viscoplastic work in the absence of large material deformation. This hypothesis is supported by scanning electron microscopy images of recovered shocked samples ([Linse, 1986](#)) and hydrodynamic parametric studies ([Conley and Benson, 1999](#)).

The overall geometry of the computational simulations presented here includes the tungsten carbide powder sample, aluminum sample plate, and lithium fluoride window as illustrated in [Fig. 1](#). In order to simplify the computations, the impactor was not included in the simulations. Instead the cover plate was modeled as a rigid boundary with a specified velocity, similar to the boundary conditions utilized by [Benson \(1995\)](#). The calculations were performed for a geometry representing a thin slice of the experiment; a 1 mm (y-direction) by 2 mm (x-direction) cavity was filled with approximately 1400 particles as described above and shown in [Fig. 3](#). All of the simulations presented here utilized identical initial grain configurations. However, simulations were performed with different initial grain configurations in order to assess the effect of variations in initial conditions. Simulations were also performed with the y-dimension increased to as large as 3 mm in order to assess the effect of the lateral dimension on bulk behavior. No significant deviation in the Hugoniot states achieved within the powder was observed with any of these variations. Just as in the experiments, the granular WC was backed by 1 mm of aluminum and 3 mm of lithium fluoride (LiF). For these calculations the particle diameter was 32 μm and the volume fraction of the WC was 55%. Periodic boundary conditions were utilized for the top and bottom (y-direction) of the simulation. If the boundary conditions in the y-direction were switched to solid walls, a different (typically higher) compaction wave speed resulted. A computational resolution was

selected so that at least 10 computational cells were used to represent each grain. These calculations required approximately 10 hours utilizing 8 nodes (16 processors, 3.06 GHz Intel Xenon processors with 2 GB of RAM) to advance the computational simulation to 4.5 μs .

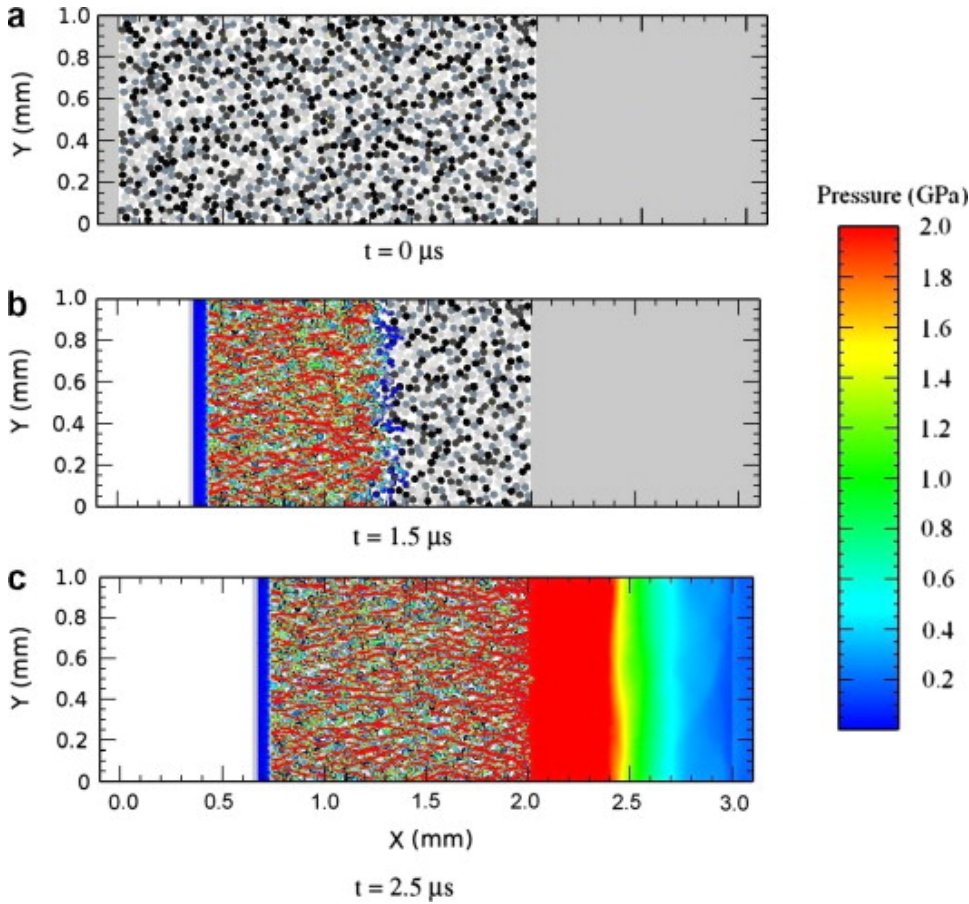


Fig. 3. Illustration of compaction wave resulting from a driver plate velocity of $u_p = 300$ m/s. Color indicates pressure contour.

Material constants utilized for these calculations are listed in [Table 1](#). A Mie-Grüneisen equation of state ([Meyers, 1994](#)) was used for all three materials included in these calculations. The equations of state parameters for WC were obtained by fitting a linear shock velocity–particle velocity ($U_s - u_p$) Hugoniot through the inelastic data reported in [Dandekar and Grady \(2001\)](#). The WC was modeled as elastic, perfectly plastic using the strength and Poisson’s ratio values from [Dandekar and Grady \(2001\)](#). Dandekar and Grady state that their results indicate that Cercom WC deforms like an elastic–plastic solid under shock wave compression. The aluminum strength was modeled using a rate dependent Johnson–Cook viscoplastic model ([Johnson and Cook, 1985](#)). The LiF material response was modeled as hydrodynamic, i.e., zero shear modulus. Both the aluminum and LiF equations of state parameters were taken from [Steinberg \(1991\)](#). The fracture strength of WC was determined from experimental spall strength measurements. [Dandekar \(2004\)](#) reported the spall strength of hot-pressed WC decline rapidly with increased stress; spall strength decreases from a value of 2.06–1.38 GPa when shocked to 3.4 and 7.2 GPa, respectively. The range of shock stress investigated here varied from 1 to 4 GPa, thus a slightly higher constant value of fracture strength, 4.0 GPa, was selected for all the work presented in this study. The fracture strength of the aluminum buffer plate was estimated from spall data presented in multiple sources ([Moshe et al., 1998](#), [Davison and Graham, 1979](#)); where the fracture strength for LiF was estimated given its low elastic limit ([Graham, 1992](#)). The sensitivity of the results presented here to fracture strength will be investigated in future work.

Table 1. Constitutive relation constants

Parameter	WC	Al	LiF
Density, ρ (g/cm ³)	15.560	2.703	2.638
Zero pressure shock speed, c_0 (km/s)	5.26	5.288	5.15
Hugoniot slope, s	1.15	1.3756	1.35
Grüneisen coefficient, $\Gamma = V\partial P/\partial E)_V$	1.0	2.14	1.690
Specific heat, C_V (J/(g-K))	0.1723	0.8617	1.9217
Yield strength, Y (GPa)	5	n/a	0
Poisson's ratio, ν	0.20	0.28	0.50
Fracture strength, p_{frac} (GPa)	4.0	0.31	0.01
Strain coefficient ^a , A (GPa)	n/a	0.26496	n/a
Strain coefficient ^a , B (GPa)	n/a	0.42642	n/a
Strain rate coefficient ^a , C	n/a	1.5×10^{-2}	n/a
Thermal exponent ^a , m	n/a	1.0	n/a
Strain exponent ^a , n	n/a	0.34	n/a

a Johnson–Cook viscoplastic model constants.

3. Results

Simulations were conducted over a range of driver plate velocities from 170 to 450 m/s. We will examine the simulation results for a driver velocity of 300 m/s in detail at the grain scale before moving on to the overall model response over a range of driver plate velocities.

3.1. Compaction phenomenology

A series of images illustrating the compaction dynamics is presented in [Fig. 3](#). For the calculations shown, the rigid driver plate has a constant particle velocity of 300 m/s traveling from left to right. As the driver plate moves into the test fixture, a compaction wave propagates through the granular tungsten carbide. [Fig. 3b](#) illustrates the material deformation and colored pressure contours 1.5 μ s after driver plate motion begins. The x-position of the compaction wave front within the granular WC is not uniform along the y-direction; instead it varies by as much as 5 particle diameters. This is similar to the several particle diameters fluctuations reported by [Baer \(2002\)](#) for HMX and stress distribution within the compaction wave fronts reported by [Benson \(1995a\)](#) for granular copper. After the compaction wave traverses the granular region, it interacts with the aluminum buffer where it transmits and reflects shock waves as shown in [Fig. 3c](#). The reflected wave, a reshock, appears in the granular WC as a region of increased pressure striations. The transmitted wave is more uniform in the aluminum buffer but some variation can be seen along the shock front near $x = 2.5$ mm.

The compaction process does not result in a uniform state within the granular material as can clearly be seen in [Figs. 3b](#) and [c](#); instead there are significant spatial variations. The existence of dynamically induced stress bridges, regions of high stress, aligned with the longitudinal direction is evident in these images. The formation, growth and development of these dynamic stress bridges (also known as force chains) are similar to those observed in quasistatic and weak shock simulations ([Bardenhagen and Brackbill, 1998](#)) as well as Hopkinson bar experiments on granular PMMA ([Roessig and Foster, 2001](#)). The formation of stress bridges observed here occurred over the entire range of driver plate velocities tested, 170–450 m/s. After compaction, the stress bridges remain stationary with respect to the distribution of material, advect with the flow and remain relatively unchanged with respect to their magnitude. In the same way that a steady state of stress is achieved behind a planar shock, the dynamically induced stress bridges persist behind the compaction wave until they are perturbed by subsequent wave interactions. These striations of high stress persisted even after

the reflected reshock from the highest driver plate velocity, 450 m/s, passed back over the granular material. Most previous observations of stress bridges have involved relatively small deformations in the particles. Here, we see that they occur under conditions of relatively large deformation, largely due to stresses bypassing persistent voids in the compacted material.

To better illustrate the behavior of the grains, the plastic deformation, and the collapse of voids, an expanded view of [Fig. 3](#) is presented in [Fig. 4](#) for two different driver plate velocities. At this enlarged scale, granular deformation can be observed. Not only do the grains plastically deform, they also exhibit bulk motion in the y -direction while filling voids. Due to the Eulerian nature of the CTH calculations, cleavage and brittle fracture are not resolved in these simulations; once the WC material yields it flows plastically with constant flow stress. The final two images show the driver plate just entering the field of view; the granular material in contact with the rigid driver and the resulting deformation can be seen in these images. Grains in contact with the driver plate tend to experience large distortions. The existence of post compaction voids is evident in the compaction wave driven by the 300 m/s driver plate, whereas the near complete removal of voids is achieved by the compaction wave driven by the 450 m/s driver plate. Even for the highest driver plate velocities investigated here, the material plots presented in [Fig. 4](#) do not exhibit large two-dimensional particle deformation as characterized by particle jetting or material velocity. Thus we expect all of the results to fall in the quasistatic compaction regime characterized by low microkinetic energy ([Benson et al., 1997](#), [Nesterenko, 2001](#)).

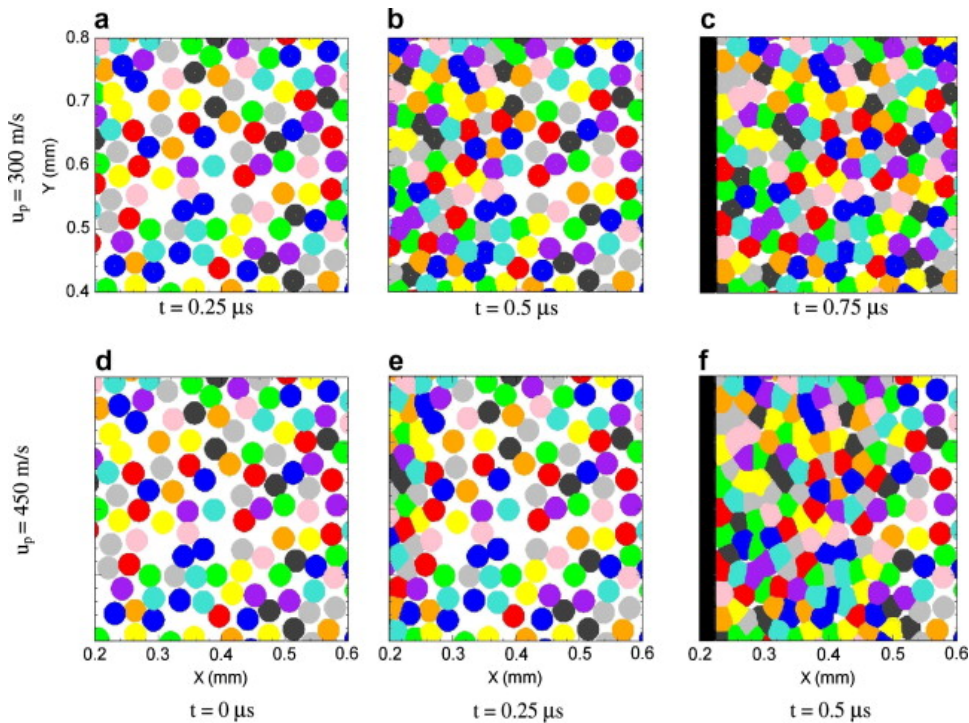


Fig. 4. Enlarged view of compaction wave for driver plate velocities of 300 and 450 m/s. Color variations are for illustration purposes only; all particles are identical.

[Fig. 5](#) presents the same three images presented in [Fig. 4](#), for the driver plate velocity of 300 m/s, with pressure contours superimposed. The highest stress levels in these images result from grains which are initially aligned and touching, as indicated in [Fig. 5a](#). The contact and transmission of grain level shock information, without the generation of release waves from free surfaces, tend to form high amplitude stress bridges. Thus, the strain energy associated with the formation of stress bridges and the subsequent plastic deformation lead to the formation of stress concentrations and eventual pore collapse. Similar behavior has been linked to the formation of hot-spots within energetic granular materials. [Baer \(2002\)](#) reported that rapid deformation occurs

at material contact points, producing large amplitude fluctuations of stress that persist over several particle diameters and that localization of energy produces hot-spots due to shock focusing and plastic work near internal boundaries as materials flows into interstitial regions. At this enlarged scale, the variation in the compaction wave is quite evident in [Fig. 5b](#); the compaction wave front location varies by approximately five grain diameters. In addition, the formation of low amplitude stress bridging preceding the compaction front in [Fig. 3b](#), can also be seen at the enlarged scale of [Fig. 5b](#). The five particle diameter wave front variation was observed to persist in the longitudinal direction throughout the compaction event.

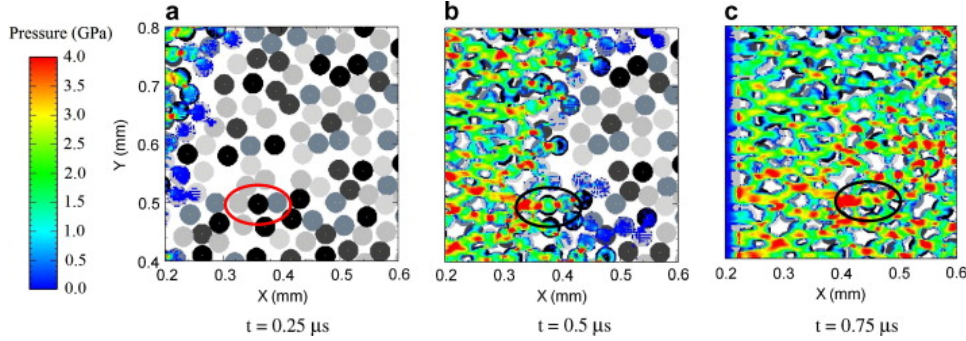


Fig. 5. Enlarged view of grain level dynamics with pressure contours superimposed. The compaction wave generates large pressure for the three particles which are initially aligned and touching. Driver plate velocity is 300 m/s.

In order to gain a better understanding of the components of stress which combine to form the compaction wave illustrated in [Fig. 5](#), the stress deviators σ'_{xx} , σ'_{yy} and σ'_{xy} are presented in [Fig. 6](#) at 0.50 μ s after impact. The stress deviators are defined as

$$\sigma'_{ij} = \sigma_{ij} - \delta_{ij}\sigma_{kk}/3, (1)$$

where δ_{ij} is the Kronecker delta, the mean stress $\sigma_{kk}/3$ is equated to negative pressure, and the summation convention is followed. As the compaction wave proceeds, there are shock and release processes occurring on the scale of the grain, which, in turn, generate large localized normal and shear stress distributions. [Fig. 6](#) demonstrates that, although the predominate longitudinal stress is compressive, there are complex shock and rarefaction interactions on the order of the grain. These shock and release processes tend to occur more during the initial loading of the grains near the compaction wave front. These processes occur rapidly on a granular level, as compared to the compaction wave which proceeds relatively slowly through the bulk material. These shock induced grain level processes can also be observed in the lateral stress, σ_{yy} , where both compressive and tensile lateral stresses are generated near the compaction wave front. Within the compaction front, high amplitude localized tensile stresses can be achieved. The maximum localized tensile stress achieved in this simulation is 3.8 GPa; however tensile stresses rarely exceeded 3 GPa. These stresses approach the specified fracture strength of 4 GPa. The rapid variation in stress at the grain level could be a major contributor to brittle granular fracture observed in experiments involving ceramic materials ([Meyers et al., 1999](#)). The formation of the strong stress bridge pointed out in [Fig. 5](#) can also be observed in [Figs. 6a](#) and [b](#).

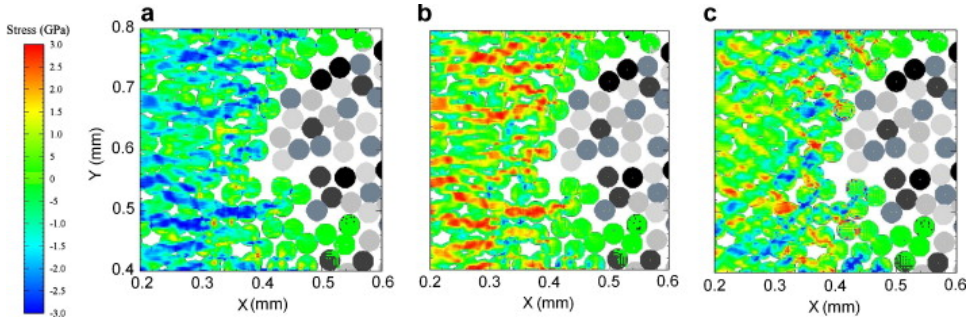


Fig. 6. Enlarged view of compaction wave with stress deviator magnitude (a) σ_{xx}' , (b) σ_{yy}' and (c) σ_{xy}' contours superimposed 0.50 μ s after driver plate motion at 300 m/s begins.

[Fig. 6c](#) shows the formation of positive and negative shear stresses, σ_{xy} , stress induced by the wave traveling in the x-direction. The y-direction momentum transport mechanism comes about as a result of microscopic particulate interactions represented by the elastic–plastic constitutive relation combining with the variations in dynamic grain surface boundary conditions and off-axis loading. If the WC samples were fully consolidated and isotropic before compaction, there would be no induced shear stress, σ_{xy} . Thus the induced stress represents a deviation from one-dimensional shock conditions and continuum behavior. The local deviatoric shear stress is of the order of the lateral and longitudinal normal stresses. Thus the sub-grain diffusion of momentum is a significant mechanism during the compaction of granular WC. As with the normal stresses, the magnitude of the shear stress appears to be highest near the leading edge of the compaction wave where most material deformation takes place.

3.2. Averaged compaction phenomenology

Averaging a solution variable, $\Phi(x,y)$, was accomplished by integrating across a column of cells of the solution domain parallel to the shock front, given as,

$$\bar{\Phi}_m(x) = \frac{1}{\ell} \int_0^\ell \Phi(x,y) dy, \quad (2)$$

where ℓ is the vertical dimension of the domain. [Fig. 7](#) presents the averaged stress states, as denoted with an overbar, as a function of x-position at three separate times for a drive plate velocity of 300 m/s. Averaging in the y-direction allows one to compare the resulting mesoscale calculations to a one-dimensional shock formulation applied to the bulk powder. Averaged normal stresses, $-\bar{\sigma}_{xx}$ and $-\bar{\sigma}_{yy}$, are compressive and therefore negative; however, $-\bar{\sigma}_{xx}$ and $-\bar{\sigma}_{yy}$ are presented for simplicity. The averaged pressure (mean stress) signature is presented along with the normal stresses for comparison. Since the local shear stress, σ_{xy} , changes sign, the magnitude of the shear stress was averaged for presentation in [Fig. 7](#).

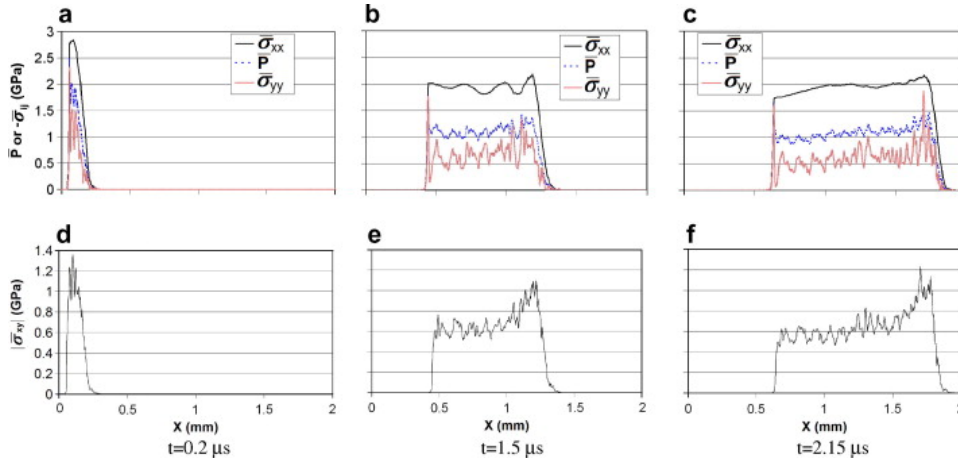


Fig. 7. Pressure and stress of compaction wave averaged in the y -direction versus grain bed position for a driver plate velocity of 300 m/s.

The average stress behind the compaction wave front does not immediately attain a steady value upon driver motion. The amplitude of the normal stresses behind the compaction wave initially increases and then decreases to a quasi-steady value as the wave propagates into the grain bed. Particularly large stresses are induced in the grains near the driver plate interface because of its rigid nature. Grains adjacent to the driver plate experience large lateral deformation and stress, not only in the averaged σ_{yy} stress signature presented in Fig. 7, but also locally in the material plots presented in Fig. 4c and the pressure plots of Fig. 5c. As the compaction wave propagates through the granular material, the averaged stress behind the compaction front fluctuates until it reaches a quasi-steady value. From Fig. 7b it appears that the quasi-steady state longitudinal stress, $-\sigma_{xx}$, is approximately 1.94 GPa, whereas the average lateral stress, $-\sigma_{yy}$, is approximately, 0.79 GPa and the averaged magnitude of the quasi-steady state shear stress is 0.60 GPa. The rise time, t_s , associated with the steady longitudinal stress, $-\sigma_{xx}$, presented in Fig. 7b is approximately 78 ns over a spatial distance of 68 μm .

As the compaction wave nears the buffer plate, the averaged normal stress state near the compaction front begins to rise. This rise in average stress appears before the compaction wave front reaches the buffer plate. Careful examination of material and pressure contour plots similar to those presented in Fig. 6 indicates that low amplitude stress bridges extending in front of the averaged compaction wave front reach the buffer plate before the main compaction wave. The resulting reshock from these stress bridges cause the rise in stress near the compaction wave leading edge as the averaged compaction wave nears the grain/buffer interface.

The averaged magnitude of shear stress presented in Figs. 7d, e and f do not propagate through the granular material as a square wave. Instead, the wave exhibits an initial rise in shear stress before decaying to a quasi-steady state value of ~ 0.6 GPa. As will be shown, the initial rise in shear stress corresponds to the portion of the compaction wave where the grains are experiencing the largest deformation and rotation.

Although the stress profiles behind the compaction wave never attain a constant value, the average stresses do oscillate about their respective quasi-steady state values. The long wavelength oscillations superimposed on the averaged longitudinal stress, visible in Fig. 7b, persist throughout the compaction event whereas the pressure, lateral stress, and shear stress all exhibit high frequency fluctuations superimposed on their respective quasi-steady values. A comparison of the averaged density and pressure in Fig. 8 reveals that these high frequency variations are similar in nature to the variability in averaged density. The average density in Fig. 8a in front of the compaction wave is $8.54 \pm 1.03 \text{ g/cm}^3$, where 1.03 g/cm^3 is the standard deviation, and $13.44 \pm 0.52 \text{ g/cm}^3$ behind the compaction wave. The average density after the reshock wave is $13.72 \pm 0.21 \text{ g/cm}^3$. The averaged density increases with each compaction process. The variability of the

averaged densities is not a smooth function of x -position before or after the arrival of the compaction wave, or after the reshock from the grain-LiF interaction. However, the variability in the density decreases with the passing of each successive compaction process by about a factor of 2. The leading edge of the compaction wave, as indicated in [Fig. 8](#), is defined as the x -position location where the averaged pressure first reaches half its quasi-steady average value, or approximately 0.60 GPa. The compaction wave front calculated in this way is located at $x = 0.42$ mm, which is consistent with the stress contours shown in [Fig. 5b](#). As illustrated by the material plots presented in [Fig. 3](#), [Fig. 4](#), voids and density gradients persist within the compacted material even after the initial compaction wave. The local density near the driver plate approaches 15 g/cm^3 , the highest recorded in the granular material for a driver plate velocity of 300 m/s. This high density near the rigid driver plate could be the source of the initial high amplitude stress presented in [Fig. 7a](#). [Fig. 8c](#) demonstrates that the effect of the reshock wave on the averaged density is minimal; the reshock is insufficient to completely close the voids within the granular material.

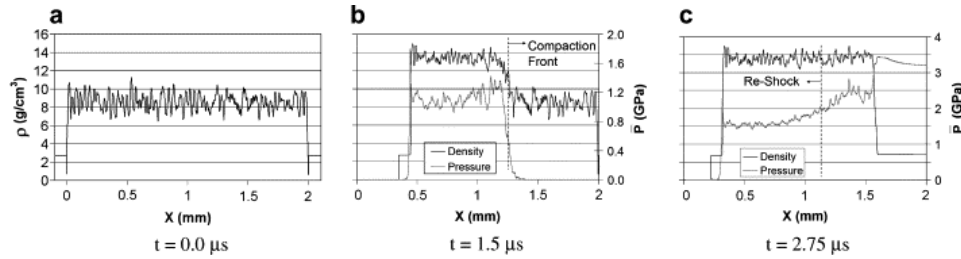


Fig. 8. Average density and pressure as a function of x - position for a driver plate velocity of 300 m/s.

The compaction wave induces spatial variations in the thermodynamic and mechanical states within the granular material, which result in grain scale transverse (y -direction) material velocities. The magnitude of the transverse velocity, averaged across the granular material in the y -direction, is presented in [Fig. 9](#). These figures indicate a significant transverse velocity near the compaction front as material moves and deforms to accommodate an efficient packing. After this initial transverse motion, the material rings back to near zero transverse velocity. The striking feature of [Fig. 9](#) is the large rise and then decline in average transverse velocity magnitude within the compaction wave front, where the peak velocity, 35 m/s, is approximately 10% of the driver plate velocity. This feature in transverse velocity roughly corresponds to the large shear stress observed in [Fig. 7b](#); as one might expect these two processes are related. The compaction wave induces a transverse velocity resulting in strong localized velocity gradients, which in turn result in strong localized shear stresses. These shear stresses decay quickly after the passage of the wave front with the reduction in transverse velocity. Similar behavior has been experimentally observed in fully dense steel with 30–80 μm grains ([Meshcheryakov and Atroshenko, 1992](#)) and in discrete element simulations on copper ([Yano and Horie, 1999](#)). In the [Meshcheryakov and Atroshenko \(1992\)](#) experiments micro-flows, including *meso*-rotations, resulted in a dispersive particle velocity centered within the shock front which was between 10 and 30% of the shock particle velocity.

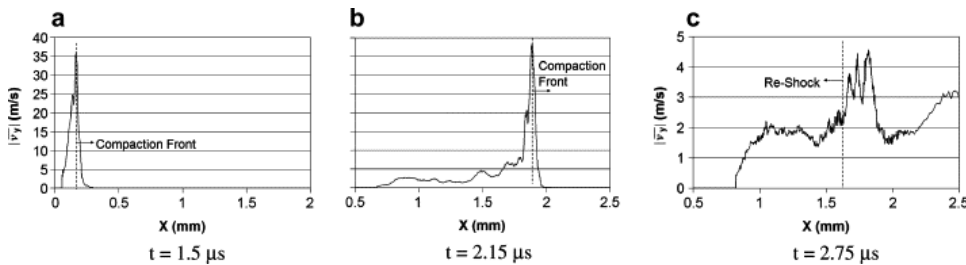


Fig. 9. Average transverse velocity magnitude at $1.5 \mu\text{s}$ after impact for a driver plate velocity of 300 m/s.

In order to better understand the transient nature of the state of stress behind the compaction wave front presented in Fig. 7, the stress signature behind the compaction wave's leading edge was averaged along the x-direction (longitudinal) to produce a single value indicative of the WC's post shock state of stress. This longitudinally averaged stress is presented as a function of the x-position of the compaction wave's leading edge in Fig. 10. As an example, the average longitudinal stress, $-\sigma_{xx}$, behind the compaction wave front presented in Fig. 7b has a value of approximately 1.94 GPa while the location of the compaction wave front is approximately 1.25 mm. Thus Fig. 10 indicates an averaged normal stress state of $-\sigma_{xx} = 1.94 \text{ GPa}$ at 1.25 mm.

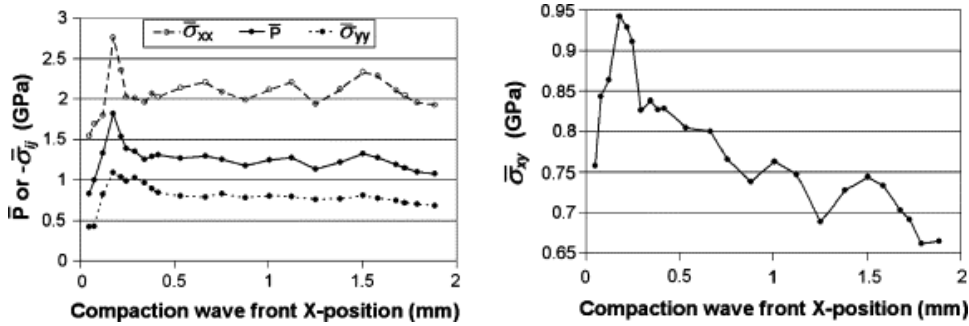


Fig. 10. Longitudinally averaged stress and pressure versus compaction wave position for a driver plate velocity of 300 m/s.

The evolution of the longitudinally averaged normal stress states presented in Fig. 10a demonstrates a nearly linear rise in amplitude followed by an asymptotic decay and oscillation. The high amplitude rise is largely due to the rigid nature of the drive plate, which deforms nearby particles more severely than material away from it. However, any boundary at the edge of the granular material (e.g., an aluminum cover plate as in the experiments) is expected to significantly perturb the material state due to phenomena such as jetting, penetration of the particles, etc. From these curves one can conclude that the bulk stresses induced in the granular materials are approximately $-\sigma_{xx} = 2.1 \text{ GPa}$, $-\sigma_{yy} = 0.80 \text{ GPa}$ and $P = 1.25 \text{ GPa}$, which are different than the values presented in Fig. 7. Averaging not only in the y-direction but also in the x-direction tends to smooth the variability in stress introduced by the material placement, i.e., the density fluctuations presented in Fig. 8. Thus it is not sufficient to determine the bulk behavior from a single snap shot in time, such as Fig. 7; one must seek a spatially (or, equivalently, temporally) averaged stress state.

The mean of the absolute value of shear stress, shown in Fig. 10b, exhibits behavior similar to the normal stresses early on, but then drops continuously. This continuous drop is a result of the initial spike in shear stress becoming a smaller component of the longitudinal average, as presented in Fig. 7b. However, from the individual wave forms, the bulk shear stress could be estimated as approximately 0.6 GPa; thus, eventually the average shear stress presented in Fig. 10b should approach 0.60 GPa. In order to verify this, a longer computational domain is required.

Since pressure is an averaged spherical stress, it exhibits smoother behavior as compared to the normal and shear stress states and might be a better indicator of the overall steadiness of the compaction wave. If the quasi-steady state pressure behind the compaction wave is assumed to be nominally 1.25 GPa, then the compaction wave propagates approximately 0.5 mm into the grain bed, or a distance of roughly 16 particle diameters, before attaining its quasi-steady state value. This is in contrast to the steady wave behavior observed in more ductile materials. Benson reported that Ni-alloy achieved steady behavior after a few particle diameters (1997) and that monosize copper and alumina achieved steady behavior after 8–10 particle diameters (1995a). Aside from material differences and the higher driver plate velocities in Benson's work, there are several numeric differences between these studies. The first is that Benson utilized a smaller computational domain

with 15 particle diameters in the shock direction, as opposed to the 50–60 particle diameters utilized here. In addition, Benson used “roller” or symmetry plane boundary conditions as opposed to the periodic boundary conditions utilized here.

In order to characterize the velocity of the compaction wave, the leading edge of the compaction wave was plotted as a function of time in [Fig. 11](#). The leading edge of the compaction wave front is defined as the location where the averaged pressure obtains half its quasi-steady value. Despite the stress transience in the initial wave behavior presented in [Fig. 7](#), the leading edge of the compaction wave travels with a nearly constant velocity of 830 m/s throughout the grain bed. The small variations above and below the linear fit appear to be caused by the stochastic nature of the granular material. The computationally derived compaction wave speed is lower than the experimentally measured compaction wave speed of 970 m/s with the same particle velocity.

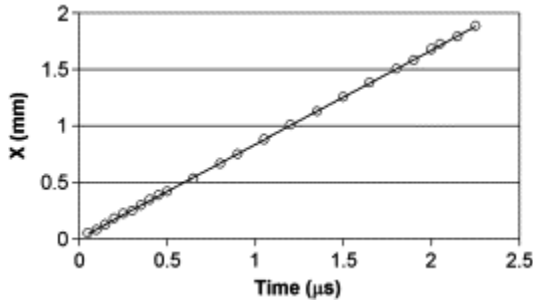


Fig. 11. Position of compaction wave front as a function of time for a driver plate velocity of 300 m/s. The best-fit linear relationship corresponds to a constant compaction wave speed of 830 m/s.

With an estimate of both the rise time and the compaction wave speed, it is possible to estimate the compaction wave thickness. Unlike the 2–5 grain variability in the location of the compaction wave, the thickness is an estimate of the distance over which the granular material is compacted. The compaction front thickness, Δ , can be estimated from the following relationship,

$$\Delta = (U_s - u_p)t_s, \quad (3)$$

where U_s , u_p and t_s are the compaction wave speed, particle velocity and rise time respectively ([Nesterenko, 2001](#)). Eq. (3) yields a compaction wave thickness of 1.7 grain diameters. [Nesterenko \(2001\)](#) reports the compaction thickness for tungsten powder, with 1000–2000 μm size grains, to be on the order of a grain diameter. Utilizing Eq. (3) and the experimental data obtained in [Vogler et al. \(2007\)](#), the shock wave thickness for WC with a grain size of 32 μm is approximately 1.3 grain diameters. Thus, the computational estimate is in good agreement with both experimental data sets.

3.3. Hugoniot response

In this section, we calculate the bulk response of the granular material in a manner similar to that used in the experiments, i.e., using the Rankine–Hugoniot relationships for conservation of mass and momentum for a steady wave. In order to calculate the compaction wave speed from the computational results in a way which is more akin to the interferometric velocity measurements made experimentally, time of arrival data is collected from multiple tracers arranged laterally at discrete longitudinal (x-position) stations. This procedure is similar to the “virtual gauge” technique implemented in hydrodynamic mesoscale calculations in order to estimate the particle velocity of shocked HMX by [Conley and Benson \(1999\)](#). At each x-position tracer station, 10 tracer points are equally spaced along the y-direction. The particle velocity at each of these 10 tracer points are averaged and the average wave profile at two different x-position stations, 0.5 mm and 1.5 mm, is presented in [Fig. 12](#) for a driver plate velocity of 300 m/s. The shaded region in [Fig. 12](#) represents the min/max envelope created by all 10 tracer points and two individual traces are presented for comparison. Due to local variations in the compaction

wave speed, each tracer point within a station records a different arrival time of the compaction wave. Variations in local compaction wave speeds are due mainly to variations in particle distribution, as shown in [Fig. 5](#), [Fig. 6](#). Clusters of particles in close proximity to each other will transmit the compaction wave information faster than particles separated by large gaps. Just as in the stress calculations presented above, arrival time is marked when the averaged particle velocity achieves half the steady state value, or 150 m/s. As can be seen in [Fig. 12](#), individual tracers do not necessarily “jump” to the particle velocity of 300 m/s. Instead they demonstrate behavior which is indicative of multiple wave interactions, they can rise, fall, or plateau before finally achieving the driver plate velocity. These multiple wave interactions become more pronounced as the compaction wave propagates along in the longitudinal direction as can be seen by comparing [Figs. 12a](#) and [b](#). This multiple wave behavior is a result of the existence of voids, grain level free surfaces, and variations in particle position relative to one another. As presented in [Fig. 5](#), [Fig. 6](#), this mesoscale shock behavior manifests itself as a non-uniform bulk compaction wave. Eventually, however, all the tracer points must equilibrate to the driver plate velocity of 300 m/s. Thus when automating a process by which to calculate the shock velocity–particle velocity relationship, it is easier and probably more reliable to utilize the particle velocity profiles as opposed to pressure or stress wave profiles.

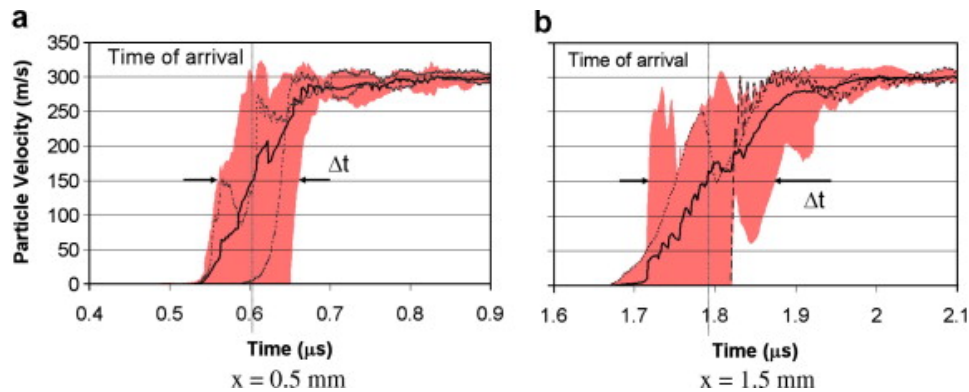


Fig. 12. Particle velocity histories for Lagrangian tracer points placed at a fixed x -position for a driver plate velocity of 300 m/s. The averaged particle velocity wave profile is presented by a solid black line, two individual tracers are presented by dashed line and the shaded region is the min/max envelope created by all 10 tracers. The compaction wave time of arrival indicated on figure is (a) 0.605 μ s, (b) 1.791 μ s.

The average times of arrival for tracer stations at 0.5 mm and 1.5 mm are indicated on [Fig. 12](#) with a dotted line and are 0.605 μ s and 1.791 μ s, respectively. By knowing the average time of arrival and the distance into the bed of the tracer station, each Lagrangian point station records a compaction wave speed; for the two x -stations presented in [Fig. 12](#) the compaction wave speeds are 826 m/s and 838 m/s, respectively. The variation in time of arrival is a measure of the computational uncertainty in the compaction wave speed. These compaction wave speeds calculated from averaged particle velocity data compare favorably to the 830 m/s compaction wave speed calculated using the pressure data.

The variation in compaction wave arrival time for a given Lagrangian station is approximately $\Delta t \sim 0.10 \pm 0.01 \mu$ s as seen in [Fig. 12](#). Once this variation is established it remains relatively constant as the compaction wave propagates in the x -direction. With a compaction wave speed of nominally 830 m/s, the variation in arrival time corresponds to a variation in the compaction wave location of approximately 2.5 grain diameters, which is consistent with [Fig. 3](#), [Fig. 5b](#).

In order to calculate the bulk compaction wave speed for a given driver plate velocity, the compaction wave speeds for all the tracer stations are ensemble averaged. With 5 x -position stations per calculation, typically, 50 tracers in all were utilized in calculating the bulk compaction wave velocity for a given driver plate velocity. This

procedure was automated and repeated over a range of driver plate particle velocities in order to construct the shock velocity–particle velocity ($U_s - u_p$) relationship for the bulk granular material presented in Fig. 13a. This is a common way of reporting the shock behavior of materials and the linear fit to this data is $U_s = 1.410 u_p + 399$ m/s. The error bars in Fig. 13a represent the minimum and maximum compaction wave speed, as calculated by the Lagrangian particle velocities, recorded within the target as described above. For a driver plate velocity of 300 m/s, the minimum and maximum compaction velocities recorded in the target were 820 and 838 m/s, respectively. As can be seen in Fig. 13a, the variation in wave speed tended to decrease as the particle velocity increased. Experimental $U_s - u_p$ data for tungsten–carbide (Vogler et al., 2007; Vogler, 2007—unpublished results) are presented along with the computational data in Fig. 13 for comparison. The experimental $U_s - u_p$ results were fit with a straight line, $U_s = 1.456 u_p + 452.8$ m/s. The slopes of the computational and experimental linear fits are quite similar, but their intercepts are about 54 m/s or 12% different. For identical initial geometry, it was found that changing the y -direction boundary conditions from periodic to symmetric resulted in a 2% increase in the compaction wave speed.

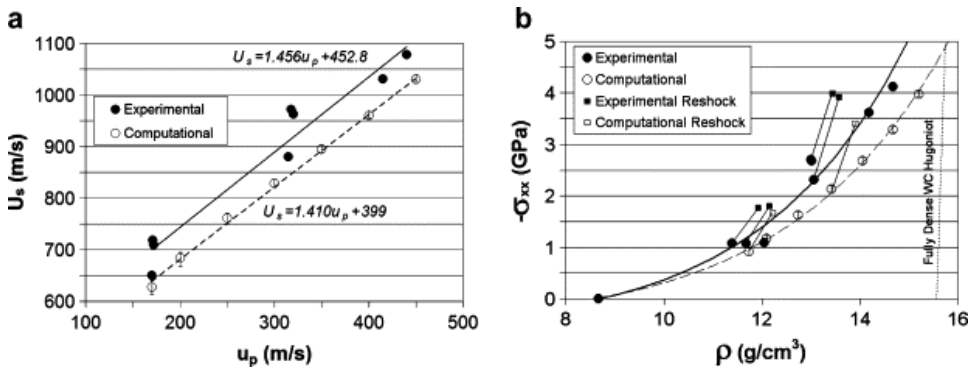


Fig. 13. Experimental and computational shock response in (a) the shock velocity–particle velocity plane and (b) the stress density plane.

With shock velocity and particle velocity known for a steady wave, it is possible to calculate the longitudinal stress using the Rankine–Hugoniot relationship from conservation of momentum

$$\sigma_{xx} = -\rho_{00} U_s u_p, \quad (4)$$

where ρ_{00} is the initial density of the undisturbed material, and the density of the shocked material from conservation of mass

$$\rho = \rho_{00} \frac{U_s}{U_s - u_p}. \quad (5)$$

The simulation results are shown in the stress–density plane in Fig. 13b; the solid and dashed lines are transformations of the best-fit experimental and computational lines of Fig. 13a to the stress–density plane using Eqs. (4), (5). The computational results are somewhat less stiff than the experimental results. From Eq. (4), the longitudinal stress for the $u_p = 300$ m/s particle velocity simulation is approximately $-\sigma_{xx} = 2.1$ GPa, which agrees well with the quasi-steady state longitudinal averaged normal stress, $-\sigma_{xx} = 2.1$ GPa, presented in Fig. 10a. The density after compaction from Eq. (5) is 13.47 g/cm³, whereas the average density presented in Fig. 8b is 13.44 ± 0.52 g/cm³. In order to further compare the experimental results obtained in Vogler et al. (2007) to the computational results obtained here, the reshock stress is presented on Fig. 13b as well. Although the reshock states under predict the experimental results, the relative increase in the reshock stress as well as the Rayleigh paths taken to achieve the reshocked state in the computational and experimental results are similar. Both the experimental and numerical results indicate that the reshock state lies above the Hugoniot. The

mechanism governing the reshock and the apparent strengthening of the granular bed are not well understood. The simulations of the WC were carried out using a simple Mie-Grüneisen equation of state with a static yield condition, thus neither phase change nor strain-hardening of the WC are responsible for the reshock states lying above the principle Hugoniot.

3.4. Wave front characterization

In order to characterize the behavior of the wave front several metrics were explored. [Swegle and Grady \(1985\)](#) found that steady waves in many fully dense materials exhibit a power law relationship between stress and strain, $\epsilon \propto \sigma^n$, where n is approximately four. This empirical relationship was measured for granular tungsten carbide to be $\epsilon \propto \sigma^{1.2}$ ([Vogler et al., 2007](#)) and the exponent was approximately 1.0 for TiO_2 data from the literature ([Anderson et al., 1994](#)). The current mesoscale computational results were fit to the same empirical relationship in order to directly compare the experimental and computational results as shown in [Fig. 14](#).

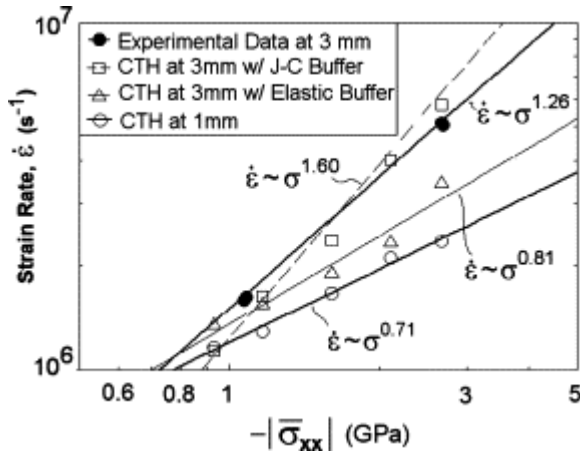


Fig. 14. Strain rate–stress relationship for experiments and simulations.

The strain rate–stress relationship was experimentally determined at the interface between the sample buffer plate and the lithium fluoride window at $x = 3$ mm (see [Fig. 1a](#)). The strain rate–stress relationship was numerically determined at various positions of the mesoscale model. First, the relationship was calculated within the powder at $x = 1$ mm by fitting ensemble averaged stress wave profiles from tracers points located along the y -direction yielding an exponent of $n = 0.7$. Since the magnitude of the stress wave transmitted into the sample buffer plate exceeds the Hugoniot elastic limit (HEL) of aluminum, the transmitted wave separates into elastic and plastic (bulk) components as it traversed the buffer plate. The baseline calculations were performed for an aluminum buffer plate with Johnson–Cook (J–C) viscoplastic behavior. The calculated wave profiles, after they were transmitted through the buffer plate, were fit to the strain rate–stress relationship with a resulting stress exponent of $n = 1.6$. Thus the wave profiles significantly steepened as a result of the nonlinearity associated with the wave interaction with the aluminum buffer. To minimize effects of the wave evolution in the aluminum buffer, additional calculations were performed with a buffer plate that remained elastic over the stress range of interest. In these simulations, the waves did not steepen as drastically and a stress exponent of $n = 0.8$ resulted. Even though the resulting exponents from these various simulations do not match the experimentally determined exponent, the simulations of the granular compaction follow the power law relationship suggested by [Swegle and Grady \(1985\)](#). Improvements to numeric simulations might be obtained if additional physical phenomena such as contact, sliding, friction, and fracture were included.

[Fig. 9](#) demonstrated that the compaction wave front induces significant mean transverse or y -velocity magnitude, $|v_y|$, which then quickly decays. This process occurs even though the mean transverse velocity, v_y , at any given x -position is near zero. In order to gain a better understanding of the induced transverse

momentum as a result of the grain interactions within the compaction wave front, the transverse velocity was statistically investigated. The computational calculations presented above were performed using 400 computational cells in the y -direction; however only data obtained from computational cells containing material were investigated (i.e., void spaces were ignored) resulting in approximately 300 y -velocity data points per x -position. In order to assess the steadiness of the compaction wave, the mean and standard deviation of the transverse velocity magnitude at the compaction front, $|v_y|$, was calculated as the compaction wave propagated through the grain bed. The means are presented in Fig. 15a as a function of x -position, where the error bars represent one standard deviation. The gray area superimposed on Fig. 15a indicates the space bound by the minimum standard deviation from the mean $|v_y|$ over the entire x -range. This illustrates that the mean transverse velocity magnitude remains bound by the light gray area in Fig. 15a. and therefore appears to be steady as it propagates through the grain bed.

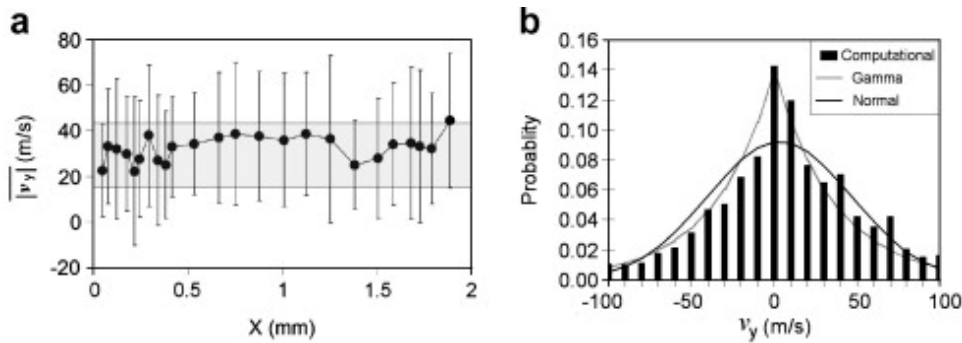


Fig. 15. Statistical view of compaction wave front (a) mean and standard distribution of lateral velocity magnitude (b) probability density functions of lateral velocity.

The transverse velocity, v_y , at the compaction wave front for the entire computational domain was fit to a variety of probability density functions with twenty evenly spaced bins and a minimum of 30 occurrences in each bin using the Matlab statistical toolbox (MATLAB, 2004). Fitting all of the mean transverse velocities with one distribution is justified given the wave steadiness found in Fig. 15a. Two of the resulting distributions, normal and gamma, as well as the computational data, are presented in Fig. 15b for comparison. As expected, the distribution of the transverse velocity, v_y , is centered about zero. The normal distribution presented in Fig. 15a has a mean of 3.2 m/s and a standard deviation is 43 m/s, where as the gamma distribution has an alpha of 1 and a beta of 3600. The Kolmogorov–Smirnov goodness-of-fit test with a 5% significance level was applied to these two distributions (Harnet, 1975). The normal distribution failed this test while the gamma distribution passed. Except for the large number of occurrences near zero, the data appears normal.

The average transverse velocity magnitude through the entire compaction event is 31 m/s; the mean transverse velocity magnitude varies from 22 to 44 m/s, with an overall standard deviation of approximately 26 m/s. This overall average of 31 m/s suggests that approximately 10% of the momentum in the shock front is redirected to the transverse direction. This transverse momentum contributes to the generation of local shear stresses, granular frictional heating, and other forms of internal dissipation.

Multiple grain realizations were generated and utilized as initial conditions for this study. The compaction wave speed measured in different initial grain configurations, with statistically identical initial conditions, was within the variations measured in a single grain realization measured at different axial locations. The statistical analysis presented above was performed for one simulation, the 300 m/s driver plate simulation. An assessment as to the stationary nature of the compaction wave could be determined by performing multiple engagements for different powder arrangements. The statistical analysis performed here took an alternative approach by

sampling the same engagement at 24 different axial locations. This is effectively the same as sampling at a fixed location for 24 different simulations with different powder arrangements. Since the grain beds are randomly filled and the compaction wave has attained a steady profile, sampling the induced lateral velocity further along in the longitudinal direction is equivalent to sampling the lateral velocity at fixed position in simulations with differing grain arrangement.

4. Discussions and conclusions

The dynamic compaction of granular ceramics is a complicated process which involves phenomenology at multiple length scales: molecular, micro, and bulk. In order to gain a better understanding of some of these processes, phenomena resolved to the grain level were investigated in two-dimensional numeric simulations using an Eulerian code.

It was found that the variations in material state induced by the compaction wave included an initial transience spanning approximately 16 particle diameters in the longitudinal direction. Thus, simulations utilizing tens or even hundreds of grains may not provide an adequate distance for this transience to pass and, therefore, might be ill suited for resolving bulk behavior. Even after this initial transience, the post-compaction state of the granular material varied about a quasi-steady state value. Thus, when seeking bulk information from a mesoscale simulation, it is not enough to look at a single snap shot in time; one must seek spatially and temporally averaged quantities. However, there are many aspects of material behavior (e.g., initiation of energetic materials through hot spot formation, localization of deformation, and fracture) that are controlled not by the average response but by the extreme values achieved within the matrix distribution. In these cases, the nature of the initial material distribution, as well as hysteresis due to loading and unloading, play an important role, even if it is secondary to the average state. Thus great care must be taken when making generalizations from micro to bulk behaviors.

Careful examination of the compaction wave indicates that it is composed of a combination of wave interactions including shock, release and momentum transport phenomenology. Grains initially in contact rapidly transmit shock information and form dynamic stress bridges which can extend up to 5 grain diameters in front of the compaction wave and persist after the compaction wave front passes, causing large variability in the location of the compaction front and post shock state. Although these stress bridges precede the arrival of the compaction wave, they do not result in large scale deformation; material deformation occurs over a shorter length scale. Shock processes have thicknesses on the order of tens of mean free paths in gases ([Bird et al., 2002](#)), on the order of a few times the mean atomic spacing for single crystals ([Meyers, 1994](#)), or on the order of the grain for solids with microstructure ([Holian, 2002](#), [Vogler and Clayton, 2007](#)). The compaction process for a porous granular material is comparatively large, on the order of the grain diameter. The average compaction wave thickness, calculated with a driver plate particle velocity of 300 m/s, is approximately 1.7 grains diameters, which is in good agreement with the experimental result of 1.3 grain diameters.

Transmission of the compaction wave through the granular material is a complicated process. In addition to the dynamic stress bridges, momentum transport plays a key role. In the two-dimensional calculations performed here, grains not initially in contact must rely on momentum transport to close the gaps and carry the compaction process forward. The velocity of the grains, and therefore the velocity of the compaction wave through the void space, is on the order of the particle velocity of the driver plate, whereas the transmission velocity associated with the formation of stress bridges occurs on the order of the shock velocity of the bulk material. Each of the transport mechanisms, momentum and shock, has an associated time scale. The combination of differing transport mechanisms results in a compaction wave through a granular material that is much slower than a shock traversing its fully dense counterpart. Although local variations were observed, the compaction wave velocity remained relatively constant as it traversed the grain bed.

Complete densification was not achieved, even for the highest driver plate velocities investigated. As a result, the compaction wave did not produce a constant material state; temporal and spatial variations in stress and density persisted in the post compacted material. These variations result not only from multiple wave and transport mechanisms traversing a random grain distribution but also the existence of voids in the post compaction state. The compaction process, over the stress regime investigated here, results in a quasistatic compact as defined by [Nesterenko \(2001\)](#). The fact that no jetting or vortices were observed in these calculations is a result of the high strength and density of the underlying material; much more energy would be required to fully compact the material. The numeric simulations indicate that complete compaction would occur near stress levels of 5 GPa; however, it is clear from the experimental Hugoniot data that the material stress levels would have to be much higher. Although averaged quantities such as stress and density qualitatively match experimental results, the numeric simulations tend to under predict the stress–density Hugoniot.

The simulations accurately predicted the slope s for the linear U_s-u_p relationship but under predicted the zero pressure shock speed, c_0 , by 12%. Experimental data for both porous tungsten ([Trunin et al., 1989](#)) and porous tantalum carbide ([Marsh, 1980](#)) demonstrate that the zero pressure shock speed is a strong function of initial bulk density, ρ_{00} . In contrast, the Hugoniot slope s is nearly invariant to initial bulk density. These experimental data demonstrate that changes in bulk density result in a nearly linear change in the zero pressure shock speed for porous tungsten. The tungsten data resulted in the following relationship: $\Delta\rho_{00} = 7.4 \Delta C_0$, where $\Delta\rho_0$ is in units of g/cm^3 and ΔC_0 is in units of km/s . From this relation, the 12% difference between the experimental and numeric zero pressure shock speed, or $\Delta C_0 = 54 \text{ m/s}$, corresponds to a small change in initial density, $\Delta\rho_{00} = 0.38 \text{ g/cm}^3$. This change is small compared to the measured initial density of approximately $\rho_{00} \sim 8.3 \text{ g/cm}^3$. Thus the difference between the experimental and numerical zero pressure shock speed could be due to small density variations. Owing to the possible variations in material distributions and the inability of a two-dimensional calculation to capture out-of-plane shock phenomenology, this variation in zero pressure shock speed may be not properly resolved without performing three-dimensional calculations. Other mechanisms missing from these simulations (e.g., realistic fracture and contact) may also play a role in the discrepancy between simulations and experiments.

The average stress state achieved within the granular material for a driver plate velocity of 300 m/s is $-\sigma_{xx} = 2.1 \text{ GPa}$, $-\sigma_{yy} = 0.80 \text{ GPa}$ and $|\sigma_{xy}| = 0.60 \text{ GPa}$. It is interesting to note that the averaged shear stress could be approximated from the normal stress as,

$$|\sigma_{xy}| \cong \frac{1}{2} (|\sigma_{xx}| - |\sigma_{yy}|). \quad (6)$$

This indicates that the principle stress axis is, on average, approximately 45° from the longitudinal direction. This is an interesting observation which could be utilized in the formation of a more complete state of stress within a continuum model formulation. Whether this is a result of the granular material geometry, i.e., all grains being the same size, or true of granular materials in general, will be investigated in future work.

The steady wave empirical strain rate–stress relationship $\dot{\epsilon} \propto \sigma^n$ was fit to the computational data in order to compare the compaction dynamics within the wave front to experimental results. The strain–rate stress exponent within the granular material was $n = 0.7$ and steepened to 1.6 by the time it reached the buffer-lithium fluoride interface, values that are similar to those found experimentally for porous WC and TiO_2 but very different from the value of 4 seen for a broad range of fully-dense materials ([Sweogle and Grady, 1985](#)). A statistical investigation of the transverse velocity indicates that non-Gaussian processes are occurring within the compaction wave front as grains are deformed and rearrange. The granular motion in the compaction front leads to a process whereby approximately 10% of the longitudinal momentum in the shock front is transported to the lateral direction, which represents a significant dissipation mechanism.

For the calculations presented here, no effort was made to optimize the input parameters to match experimental data; instead, in future publications we will examine the effects of model parameters such as constitutive behavior for granular WC, grain shape, particle size and arrangement distribution, and dimensionality of the simulations. Of interest are the effects of these parameters not only on the overall bulk response but also on the distributions of states that describe the compacting material. Additional experimental and numerical studies on granular ceramics other than WC will help us improve our understanding of the dynamic behavior of this class of materials. Eventually, it would be valuable to perform similar calculations using a different numerical approach to study the effects of phenomena such as inter-granular friction and granular fracture, which cannot currently be captured with the Eulerian code used here.

5. Future work

There is much opportunity to further explore and probe the internal dynamics associated with the shock compaction of granular ceramic materials using mesoscale calculations. With an understanding of the limitations and accuracy of the current methodology we are planning the following future work. In order to better understand the variations in the solution as a result of the initial geometry several grain shapes will be explored including triangular and square grains. This morphology study will include grain size distribution variations, as well as, grain order variations. This study will eventually lead to a better understanding of the required fidelity of material distributions and the importance of identifying significant features in the initial geometry. A parametric study of the mechanical and thermodynamic material properties will be conducted in order to assess the sensitivity of the mesoscale simulations to various initial conditions. We expect strength to play a major role in the bulk material behavior whereas we expect dynamic fracture strength to be secondary in its effect. In addition to these parametric studies, the authors intend to investigate alternate numeric formulations which are more appropriate to model phenomena not included in this work such as grain contact and fracture. A leading candidate for this work is the computational code EMU, which is a peridynamics code currently under development at Sandia National Laboratories ([Silling, 2000](#), [Demmie and Silling, 2007](#)). The ultimate goal is to understand the compaction dynamics of loose granular ceramic materials, to determine the measurements necessary to model these materials under extreme loading conditions and to make accurate predictions with little to no experimentation.

Acknowledgments

The authors thank Scott Alexander at Sandia for his help with various routines within CTH. Sandia is a multiprogram laboratory operated by Sandia Corporation, a Lockheed Martin Company, for the United States Department of Energy's National Nuclear Security Administration under contract DE-AC04-94AL85000.

References

- [Anderson et al., 1994](#) M.U. Anderson, G.T. Holman, R.A. Graham. **Time-resolved shock compression of porous rutile: wave dispersion in porous solids**. High-Pressure Science and Technology, American Institute of Physics, NY (1994), pp. 1111-1114
- [Baer, 2002](#) M.R. Baer. **Modeling heterogeneous energetic materials at the mesoscale**. Thermochimica Acta, 384 (2002), pp. 351-367
- [Baer and Trott, 2002](#) Baer, M.R., Trott, 2002. Mesoscale descriptions of shock loaded heterogeneous porous materials. In: Furnish, M.D., Thadhani, N.N., Horie, Y. (Eds.), Shock Compression of Condensed Matter—2001, pp. 713–716.
- [Bardenhagen and Brackbill, 1998](#). S.G. Bardenhagen, J.U. Brackbill. **Dynamic stress bridging in granular material**. Journal of Applied Physics, 83 (1998), pp. 5732-5740

- [Benson, 1994](#) D.J. Benson. **An analysis by direct numerical simulation of the effects of particle morphology on the shock compaction of copper powder.** Modelling and Simulation in Materials Science and Engineering, 2 (1994), pp. 535-550
- [Benson, 1995a](#) D.J. Benson. **The calculation of the shock velocity– particle velocity relationship for a copper powder by direct numerical simulation.** Wave Motion, 21 (1995), pp. 85-99
- [Benson et al., 1995b](#) D.J. Benson, .W. Tong, G. Ravichandran. **Particle-level modeling of dynamic consolidation of Ti-SiC powders.** Modelling and Simulation in Materials Science and Engineering, 3 (1995), pp. 771-796
- [Benson et al., 1997](#) D.J. Benson, V.F. Nesterenko, F. Jonsdottir, M.A. Meyers. **Quasistatic and Dyanmic Regimes of Granular Material Deformation Under Impulse Loading.** Journal of the Mechanics and Physics of Solids, 45 (1997), pp. 1955-1999
- [Benson and Conley, 1999](#) D.J. Benson, P. Conley. **Eulerian finite-element simulations of experimentally acquired HMX microstructures.** Modelling and Simulation in Materials Science and Engineering, 7 (1999), pp. 333-354
- [Benson et al., 2001](#) Benson, D.J., Do, I., Meyers, M.A., 2001. Computational modeling of shock compression of powders. In: Furnish, M.D., Thadhani, N.N., Horie, Y. (Eds.), Shock Compaction of Condensed Matter—2001, pp. 1087–1092.
- [Bird et al., 2002](#) R.B. Bird, W.E. Stewart, E.N. Lightfoot. **Transport Phenomena.** (2nd ed.), Wiley Press (2002) pp. 350–353
- [Bourne, 2005](#) Bourne, N.K., 2005. Modelling the shock response of polycrystals at the mesoscale. In: Furnish, M.D., Elert, M., Russell, T.P., White, C.T. (Eds.), Shock Compaction of Condensed Matter—2005, pp. 307–310.
- [Carroll and Holt, 1972](#) M.M. Carroll, A.C. Holt. **Static and dynamic pore-collapse relations for ductile porous materials.** Journal of Applied Physics, 43 (1972), pp. 1626-1635
- [Carroll et al., 1986](#) M.M. Carroll, K.T. Kim, V.F. Nesterenko. **The effect of temperature on viscoplastic pore collapse.** Journal of Applied Physics, 59 (6) (1986), pp. 1962-1967
- [Case and Horie, 2005](#) Case, S., Horie, Y., 2005. Mesoscale modeling of the response of alumina. In: Furnish, M.D., Elert, M., Russell, T.P., White, C.T. (Eds.), Shock Compaction of Condensed Matter—2005, pp. 299–302.
- [Conley and Benson, 1999](#) P.A. Conley, D.J. Benson. **An estimate of the linear strain rate dependence of octahydro-1,3,5,7-tetranitro-1,3,5,7-tetrazocine.** Journal of Applied Physics, 86 (1999), pp. 6717-6728
- [Crawford, 2005](#) D.A. Crawford. **Using mesoscale modeling to investigate the role of material heterogeneity in geologic and planetary materials.** M.D. Furnish, M. Elert, T.P. Russell, C.T. White (Eds.), Shock compression of Condensed Matter—2005, AIP press (2005), pp. 1453-1457
- [Dandekar, 2004](#) Dandekar, D.P., 2004. Spall strength of tungsten carbide, Army Research Laboratory, ARL-TR-3335.
- [Dandekar and Grady, 2001](#) Dandekar, D.P., Grady, D.E., 2001. Shock equation of state and dynamic strength of tungsten carbide, In: Furnish, M.D., Thadhani, N.N., Horie, Y. (Eds.), Shock Compression of Condensed Matter—2001, pp. 783–786.
- [Davison and Graham, 1979](#) L. Davison, R.A. Graham. **Shock Compression of Solids.** Physics Reports, 55 (1979), pp. 255-379
- [Demmie and Silling, 2007](#) P.N. Demmie, S.A. Silling. **An approach to modeling extreme loading of structures using peridynamics.** Journal of Mechanics of Materials and Structures, 2 (2007), pp. 1921-1946
- [Do and Benson, 2001](#) I.P.H. Do, D.J. Benson. **Micromechanical modeling of shock-induced chemical reactions in heterogeneous multi-material powder mixtures.** International Journal of Plasticity, 17 (2001), pp. 641-668
- [Graham, 1992](#) R.A. Graham. **Solids under high-pressure shock compression.** Springer -Verlag, New York, Inc (1992)

- [Hae-Jin et al., 2005](#) C. Hae-Jin, R. Austin, J.K. Allen, D.L. McDowell, F. Mistree, D.J. Benson. **An approach for robust design of reactive powder metal mixtures based on non-deterministic micro-scale shock simulation.** Journal of Computer-Aided Materials Design, 12 (2005), pp. 57-85
- [Harnet, 1975](#) D.L. Harnet. **Introduction to Statistical Methods.** Addison Wesley Publishing, Reading Massachusetts (1975)
- [Holian, 2002](#) Holian, B.L., 2002. What is a shock wave? The view from the atomic scale. In: Horie, Y., Davison, L., Thadhani, N.N. (Eds.), High-Pressure Shock Compression of Solids VI, pp. 149–168.
- [Horie and Yano, 2001](#) Horie, Y., Yano, K., 2001. Non-equilibrium fluctuations in shock compression of polycrystalline α -iron. In: Furnish, M.D., Thadhani, N.N., Horie, Y. (Eds.), Shock Compaction of Condensed Matter—2001, pp. 553–556.
- [Johnson and Cook, 1985](#) G.R. Johnson, W.H. Cook. **Fracture characteristics of three metals subjected to various strains, strain rates, temperatures and pressures.** Engineering Fracture Mechanics, 21 (1985), pp. 31-48
- [Linse, 1986](#) V. Linse. **Metallurgical Applications of Shock-Wave and High Strain Rate Phenomena.** Dekker (1986). pp. 29–55
- [Lowe and Greenaway, 2005](#) C.A. Lowe, M.W. Greenaway. **Compaction processes in granular beds composed of different particle sizes.** Journal of Applied Physics, 98 (2005), p. 123519
- [Marsh, 1980](#) S.P. Marsh. **LASL Shock Hugoniot Data.** University of California Press (1980)
- [MATLAB, 2004](#) MATLAB, 2004. www.mathworks.com. MATLAB Version 7.0.0.19920 (R14).
- [McGlaum et al., 1990](#) J.M. McGlaum, S.L. Thompson, M.G. Elrick. **CTH: A three-dimensional shock wave physics code.** International Journal of Impact Engineering, 10 (1990), pp. 351-360
- [Menikoff, 2001](#) R. Menikoff. **Compaction wave profiles: Simulations of gas gun experiments.** Journal of Applied Physics, 90 (2001), pp. 1754-1760
- [Meshcheryakov and Atroshenko, 1992](#) Y.I. Meshcheryakov, S.A. Atroshenko. **Dynamic rotations in crystals.** Russian Physics Journal, 35 (1992), pp. 385-399
- [Meyers, 1994](#) M.A. Meyers. **Dynamic Behavior of Materials.** Wiley-Interscience, New York (1994)
- [Meyers et al., 1999](#) M.A. Meyers, D.J. Benson, E.A. Olevsky. **Shock consolidation: microstructurally-based analysis and computational modeling.** Acta Materialia, 47 (1999), pp. 2089-2108
- [Milne et al., 2005](#) Milne, A.M., Bourne, N.K., Millett, J.C.F. On the un-reacted Hugoniot of three plastic bonded explosives. In: Furnish, M.D., Elert, M., Russell, T.P., White, C.T. (Eds.), Shock Compaction of Condensed Matter—2005, pp. 175–178.
- [Moshe et al., 1998](#) E. Moshe, S. Eliezer, E. Dekel, A. Ludmirsky, Z. Henis, M. Werdiger, I.B. Goldberg. **An increase of the spall strength in aluminum, copper, and Metglas at strain rates larger than 10^7 s^{-1} .** Journal of Applied Physics, 83 (1998), pp. 4004-4011
- [Nesterenko, 2001](#) V.F. Nesterenko. **Dynamics of Heterogeneous Materials.** Springer, New York (2001)
- [Nieh et al., 1996](#) T.G. Nieh, P. Luo, W. Nellis, D. Lesuer, D. Benson. **Dynamic compaction of aluminum nanocrystals.** Acta Materialia, 44 (1996), pp. 3781-3788
- [Roessig and Foster, 2001](#) Roessig, K.M., Foster, J.C., 2001. Experimental simulations of dynamic stress bridging in plastic bonded explosives. In: Furnish, M.D., Thadhani, N.N., Horie, Y. (Eds.), Shock Compaction of Condensed Matter—2001, pp. 829–832.
- [Silling, 2000](#) A. Silling. **Reformulation of elasticity theory for discontinuities and long-range forces.** Journal of the Mechanics and Physics of Solids, 48 (2000), pp. 175-209
- [Steinberg, 1991](#) Steinberg, D.J. 1991. Equation of state and strength properties of selected materials. Lawrence Livermore National Laboratory report UCRL-MA-106439.
- [Swegle and Grady, 1985](#) J.W. Swegle, D.E. Grady. **Shock viscosity and the prediction of shock wave rise times.** Journal of Applied Physics, 58 (1985), pp. 692-701

[Tang and Wang, 2001](#) Tang, Z.P., Wang, W.W. 2001. Discrete element modeling for shock processes of heterogeneous materials. In: Furnish, M.D., Thadhani, N.N., Horie, Y. (Eds.), Shock Compaction of Condensed Matter—2001, pp. 679–684.

[Tong et al., 1995](#) W. Tong, F. Ravichandran, T. Christman, T. Vreeland. Acta Materialia, 43 (1995), pp. 230-250

[Trunin et al., 1989](#) R.F. Trunin, G.V. Simakov, Yu.N. Sutulov, A.B. Medvedev, B.D. Rogozkin, Yu.E. Fedorov.

Compressibility of porous metals in shock waves. Soviet Physics JETP, 69 (1989), pp. 580-588

[Vogler and Clayton, 2007](#) Vogler, T.J., Clayton, J.D., submitted for publication. Heterogeneous deformation and spall of an extruded tungsten alloy: plate impact experiments and crystal plasticity modeling. Journal of the Mechanics and Physics of Solids.

[Vogler et al., 2007](#) T.J. Vogler, M.Y. Lee, D.E. Grady. **Static and dynamic compaction of ceramic powders.** International Journal of Solids and Structures, 44 (2007), pp. 636-658

[Williamson, 1990](#) R.L. Williamson. **Parametric studies of dynamic powder consolidation using a particle-level numerical model.** Journal of Applied Physics, 68 (1990), pp. 1287-1296

[Yano and Horie, 1999](#) K. Yano, Y. Horie. **Discrete-element modeling of shock compression of polycrystalline copper.** Physical Review B, 59 (1999), pp. 13672-13680

Copyright © 2007 Elsevier Ltd. All rights reserved.